Appendix A

A DERIVATION OF THE PLANAR EQUATIONS OF MOTION

A.1 Newton's second law

Kinetics is the study of motion and its relationship with the forces that produce the motion (see [65]). The simplest body arising in the study of motion is a particle, or point mass, defined by Nikravesh [65] as a mass concentrated at a point. According to Newton's second law, a particle will accelerate when it is subjected to unbalanced forces. More specifically, Newton's second law as applied to a particle is

$$\vec{\mathbf{f}} = m^{(p)}\vec{\mathbf{a}} \tag{A.1}$$

where $\vec{\mathbf{f}}$, $m^{(p)}$ and $\vec{\mathbf{a}}$ respectively represents the total force acting on the particle, the mass of the particle and the acceleration of the particle (see Figure A.1).

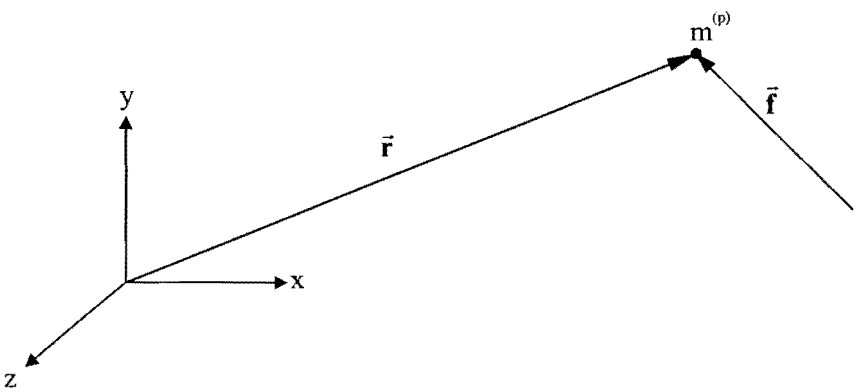

Figure A.1: A particle moving in a global coordinate system (after [65]).

Since $\vec{\mathbf{f}}$ and $\vec{\mathbf{a}}$ are three-dimensional physical vectors, they may be represented as three-vectors in the global fixed coordinate system, i.e. $\vec{\mathbf{f}} : \mathbf{f} = [f_{(x)}, f_{(y)}, f_{(z)}]^T$ and $\vec{\mathbf{a}} : \mathbf{a} = [a_{(x)}, a_{(y)}, a_{(y)}]^T$. The position vector $\vec{\mathbf{r}}$ shown in Figure A.1 locates the particle in the global coordinate system and is represented in the global reference frame by $\mathbf{r} = [x, y, z]^T$. The acceleration $\mathbf{a}$ of the particle is the second time

derivative of the position vector, i.e. $\mathbf{a} = \ddot{\mathbf{r}} = [\ddot{x}, \ddot{y}, \ddot{z}]^T$, and the global representation of expression (A.1) therefore is

$$\mathbf{f} = m^{(p)}\ddot{\mathbf{r}} \tag{A.2}$$

For a system of p particles, the application of expression (A.2) may be extended to describe the motion of each particle i, $i = 1,2,...,p$ in the system, i.e.

$$m_i^{(p)}\ddot{\mathbf{r}}_i = \mathbf{f}_i + \sum_{j=1}^{p}\mathbf{f}_{ij}\ , \ i = 1,2,...,p \tag{A.3}$$

where $\mathbf{f}_i$ is the global representation of the total externally applied force $\vec{\mathbf{f}}_i$ acting on particle i, and $\mathbf{f}_{ij}$ is the global representation of the internal force $\vec{\mathbf{f}}_{ij}$ extended by particle j on particle i. Note that $\vec{\mathbf{f}}_{ii} = \vec{\mathbf{0}}$.

Summing expression (A.3) over all p particles in the system results in

$$\sum_{i=1}^{p} m_i^{(p)}\ddot{\mathbf{r}}_i = \sum_{i=1}^{p}\mathbf{f}_i + \sum_{i=1}^{p}\sum_{j=1}^{p}\mathbf{f}_{ij} \tag{A.4}$$

and since $\vec{\mathbf{f}}_{ij} = -\vec{\mathbf{f}}_{ji}$ (Newton's third law), it follows that $\sum_{i=1}^{p}\sum_{j=1}^{p}\mathbf{f}_{ij} = \mathbf{0}$, and consequently expression (A.4) reduces to

$$\sum_{i=1}^{p} m_i^{(p)}\ddot{\mathbf{r}}_i = \sum_{i=1}^{p}\mathbf{f}_i \tag{A.5}$$

or simply

$$m\ddot{\mathbf{r}} = \mathbf{f} \tag{A.6}$$

where $m = \sum_{i=1}^{p} m_i^{(p)}$ is the total mass of the system of particles,

$\mathbf{r} = \frac{1}{m}\sum_{i=1}^{p} m_i^{(p)}\mathbf{r}_i$ is the center of mass of the system of particles, and

$\mathbf{f} = \sum_{i=1}^{p}\mathbf{f}_i$ is the total external force acting on the system of particles.

The translational equation of motion of a system of particles (A.6), also holds for a general continuous rigid body or continuum, the center of mass of which is given by

$$\mathbf{r} = \frac{1}{m}\int_{vol}\mathbf{r}^p dm \tag{A.7}$$

where $\mathbf{r}^p$ locates an infinitesimally small mass element dm as shown in Figure A.2.

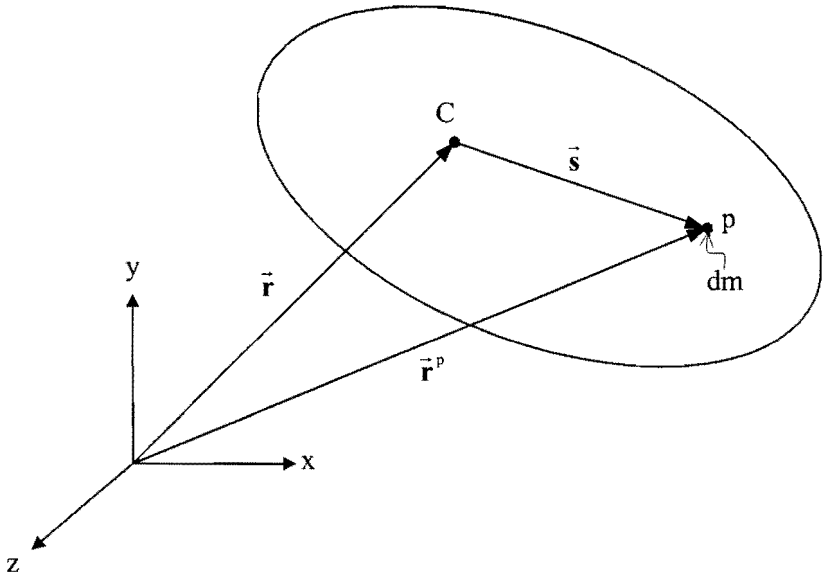

Figure A.2: A body as a collection of infinitesimally small masses (after [65]).

Since vector $\mathbf{r}^p$ is the sum of two vectors $\mathbf{r}^p = \mathbf{r} + \mathbf{s}$, it follows that

$$\begin{aligned}\mathbf{r} &= \frac{1}{m}\int_{vol}\mathbf{r}^p\,dm \\ &= \frac{1}{m}\int_{vol}(\mathbf{r}+\mathbf{s})\,dm \\ &= \mathbf{r} + \frac{1}{m}\int_{vol}\mathbf{s}\,dm\end{aligned}$$

which implies that

$$\int_{vol}\mathbf{s}\,dm = \mathbf{0} \tag{A.8}$$

and taking first and second order time derivatives gives

$$\int_{vol}\dot{\mathbf{s}}\,dm = \mathbf{0} \tag{A.9}$$

and

$$\int_{vol}\ddot{\mathbf{s}}\,dm = \mathbf{0} \tag{A.10}$$

A.2 Planar equations of motion

For the purposes of analyzing a planar machining center it is required to derive the planar equations of motion. Consider Figure A.3 showing an external force $\vec{\mathbf{f}}_i$ acting on the *i*-th particle of a system. For planar motion, the center of mass C of the system remains in the Gxy-plane, and coincides with the origin 0 of the body-fixed $\xi\eta\zeta$-coordinate system. The centroidal body-fixed $\xi\eta\zeta$-coordinate system is chosen in such a way that the ζ-axis is parallel to the z-axis. Note that the origin of the global xyz-reference frame is denoted by G.

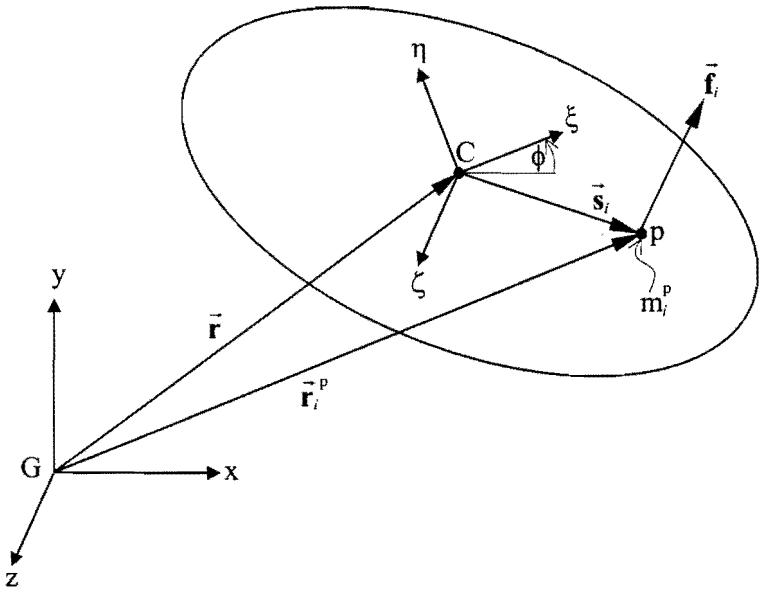

Figure A.3: Rigid body experiencing planar motion.

A.2.1 Planar translational equations of motion

The *first necessary condition* for the system in Figure A.3 to experience *planar motion* in the Gxy-plane, is that the external force $\vec{\mathbf{f}}_i$ must be parallel to the xy-plane of motion, which is only possible if the z-component $f_{i(z)}$ of the force $\vec{\mathbf{f}}_i$ is zero (see [65]).

More specifically, expression (A.6) gives the two *planar translational equations of motion*, for the system shown in Figure A.3:

$$m\ddot{x} = f_{(x)} \tag{A.11}$$

and

$$m\ddot{y} = f_{(y)} \tag{A.12}$$

with of course $\mathbf{f}_{(z)} \equiv 0$.

Expressions (A.11) and (A.12) may also be combined in matrix form:

$$\begin{bmatrix} m & 0 \\ 0 & m \end{bmatrix} \begin{bmatrix} \ddot{x} \\ \ddot{y} \end{bmatrix} = \begin{bmatrix} f_{(x)} \\ f_{(y)} \end{bmatrix} \tag{A.13}$$

with m representing the total mass of the system,

$\ddot{x}$ and $\ddot{y}$ respectively representing the x- and y-accelerations of the center of mass C, and

$f_{(x)}$ and $f_{(y)}$ respectively representing the x- and y-components of the total external force acting on the mass system.

A.2.2 Planar rotational equations of motion

The *second necessary condition* for the system in Figure A.3 to experience *planar motion*, is that it is only to rotate about the ζ-axis (see [65]). This rotation is due to the *resultant moment* about C of the external forces acting on the system. Since the ζ-axis is parallel to the z-axis, the global representation of the resultant moment of the forces about C must, for planar motion, only have a z-component.

Consider the moment about G as a result of the external forces $\vec{\mathbf{f}}_i$ and $\sum_{j=1}^{p}\vec{\mathbf{f}}_{ij}$ acting on particle i (see Figure A.3):

$$\vec{\mathbf{n}}_i^{G} = \vec{\mathbf{r}}_i^{p} \times (\vec{\mathbf{f}}_i + \sum_{j=1}^{p}\vec{\mathbf{f}}_{ij}) \tag{A.14}$$

With particle i located in the global reference frame by

$$\vec{\mathbf{r}}_i^{p} = \vec{\mathbf{r}} + \vec{\mathbf{s}}_i \tag{A.15}$$

the global representation of expression (A.15) is

$$\mathbf{r}_i^{p} = \mathbf{r} + \mathbf{s}_i \tag{A.16}$$

Hence, expression (A.14) may be represented in the global reference frame by

$$\mathbf{n}_i^{G} = \tilde{\mathbf{r}}_i^{p}(\mathbf{f}_i + \sum_{j=1}^{p}\mathbf{f}_{ij}) \tag{A.17}$$

with $\tilde{\mathbf{r}}_i^{p}$ representing the expansion of $\mathbf{r}_i^{p}$ into a skew symmetric matrix, i.e.:

$$\tilde{\mathbf{r}}_i^{p} = \begin{bmatrix} 0 & -z^{p} & y^{p} \\ z^{p} & 0 & -x^{p} \\ -y^{p} & x^{p} & 0 \end{bmatrix} \tag{A.18}$$

Substituting expression (A.3) into (A.17) yields

$$\mathbf{n}_i^{G} = \tilde{\mathbf{r}}_i^{p}(\mathbf{f}_i + \sum_{j=1}^{p}\mathbf{f}_{ij}) = \tilde{\mathbf{r}}_i^{p}(m_i^{p}\ddot{\mathbf{r}}_i^{p}) \tag{A.19}$$

Summing expression (A.19) over all $i = 1,2,...,p$, gives the sum of the moments with respect to G as

$$\mathbf{n}^{G} = \sum_{i=1}^{p}\tilde{\mathbf{r}}_i^{p}\mathbf{f}_i + \sum_{i=1}^{p}\sum_{j=1}^{p}\tilde{\mathbf{r}}_i^{p}\mathbf{f}_{ij} = \sum_{i=1}^{p}\tilde{\mathbf{r}}_i^{p}(m_i^{p}\ddot{\mathbf{r}}_i^{p}) \tag{A.20}$$

However, since $\tilde{\mathbf{r}}_i^{p}\mathbf{f}_{ij} = -\tilde{\mathbf{r}}_i^{p}\mathbf{f}_{ji}$ (see expressions (A.4) and (A.5)), it follows that $\sum_{i=1}^{p}\sum_{j=1}^{p}\tilde{\mathbf{r}}_i^{p}\mathbf{f}_{ij} = \mathbf{0}$.

Furthermore, expression (A.16) implies that

$$\tilde{\mathbf{r}}_i^{p} = \tilde{\mathbf{r}} + \tilde{\mathbf{s}}_i \tag{A.21}$$

Expression (A.20) may therefore be written as

$$\mathbf{n}^G = \tilde{\mathbf{r}}\mathbf{f} + \sum_{i=1}^{p} \tilde{\mathbf{s}}_i \mathbf{f}_i = \sum_{i=1}^{p} m_i^p \tilde{\mathbf{r}}_i^p \ddot{\mathbf{r}}_i^p \tag{A.22}$$

where $\sum_{i=1}^{p} \tilde{\mathbf{s}}_i \mathbf{f}_i = \mathbf{n}$ the sum of the moments of the external forces about C.

For a continuous body, m_i^p represents an infinitesimally small mass element dm, i.e. $m_i^p \equiv dm$, and therefore expression (A.22) becomes

$$\mathbf{n}^G = \tilde{\mathbf{r}}\mathbf{f} + \mathbf{n} = \int_{vol} \tilde{\mathbf{r}}^p \ddot{\mathbf{r}}^p dm \tag{A.23}$$

with the position of the center of mass of the continuum $\mathbf{r}$ given by expression (A.7).

Since the center of mass of the body under consideration is to remain in the Gxy-plane , the z-component of $\mathbf{r}$ is identically equal to zero, i.e. $\mathbf{r} = [x, y, 0]^T$. The expansion of $\mathbf{r}$ into a skew-symmetric matrix is therefore

$$\tilde{\mathbf{r}} = \begin{bmatrix} 0 & 0 & y^p \\ 0 & 0 & -x^p \\ -y^p & x^p & 0 \end{bmatrix} \tag{A.24}$$

The force, $\mathbf{f}$ in expression (A.23) is the global representation of the resultant external force acting on the body, and $\mathbf{n}^G$ and $\mathbf{n}$ respectively represent the resultant moment of the external forces acting on the body about the origin of the global reference frame G, and the center of mass of the body C.

In satisfying the second necessary condition for planar motion, the expansion of expression (A.23) may only yield a single non-zero scalar equation corresponding to the z-component of the resultant moment acting on the body with respect to G:

$$n_{(z)}^G = xf_{(y)} - yf_{(x)} + n_{(z)} = \left[\int_{vol} \tilde{\mathbf{r}}^p \ddot{\mathbf{r}}^p dm \right]_{(z)} \tag{A.25}$$

From expression (A.16) it follows that for a continuous body

$$\mathbf{r}^p = \mathbf{r} + \mathbf{s} = \begin{bmatrix} x \\ y \\ z \end{bmatrix} + \begin{bmatrix} s_{(x)} \\ s_{(y)} \\ s_{(z)} \end{bmatrix} \tag{A.26}$$

with first and second time derivatives given by $\dot{\mathbf{r}}^p = \dot{\mathbf{r}} + \dot{\mathbf{s}} = [\dot{x}, \dot{y}, \dot{z}]^T + [\dot{s}_{(x)}, \dot{s}_{(y)}, \dot{s}_{(z)}]^T$ and $\ddot{\mathbf{r}}^p = \ddot{\mathbf{r}} + \ddot{\mathbf{s}} = [\ddot{x}, \ddot{y}, \ddot{z}]^T + [\ddot{s}_{(x)}, \ddot{s}_{(y)}, \ddot{s}_{(z)}]^T$ respectively.

Substituting expression (A.26) into the right hand side of expression (A.25) results in

$$n^G_{(z)} = xf_{(y)} - yf_{(x)} + n_{(z)} = \left[\int_{vol} (\tilde{\mathbf{r}} + \tilde{\mathbf{s}})(\ddot{\mathbf{r}} + \ddot{\mathbf{s}}) dm \right]_{(z)} \tag{A.27}$$

From expressions (A.8) and (A.10) it follows that $\int_{vol} \tilde{\mathbf{s}}\ddot{\mathbf{r}}\, dm = \mathbf{0}$ and $\int_{vol} \tilde{\mathbf{r}}\ddot{\mathbf{s}}\, dm = \mathbf{0}$, and therefore expression (A.27) reduces to

$$n^G_{(z)} = xf_{(y)} - yf_{(x)} + n_{(z)} = x(m\ddot{y}) - y(m\ddot{x}) + \int_{vol} s_{(x)}\ddot{s}_{(y)} - s_{(y)}\ddot{s}_{(x)}\, dm \tag{A.28}$$

From expressions (A.11) and (A.12) it also follows that $xf_{(y)} - yf_{(x)} = x(m\ddot{y}) - y(m\ddot{x})$, and therefore (A.28) becomes

$$n_{(z)} = \int_{vol} [s_{(x)}\ddot{s}_{(y)} - s_{(y)}\ddot{s}_{(x)}]\, dm \tag{A.29}$$

For general three-dimensional motion, the above argument would give

$$\mathbf{n} = \int_{vol} \tilde{\mathbf{s}}\ddot{\mathbf{s}}\, dm \tag{A.30}$$

where $\tilde{\mathbf{s}}$ represents a skew-symmetric matrix of the form

$$\tilde{\mathbf{s}} = \begin{bmatrix} 0 & -s_{(z)} & s_{(y)} \\ s_{(z)} & 0 & -s_{(x)} \\ -s_{(y)} & s_{(x)} & 0 \end{bmatrix} \tag{A.31}$$

Nikravesh [65] shows that

$$\tilde{\mathbf{s}}\ddot{\mathbf{s}} = -\tilde{\mathbf{s}}\tilde{\mathbf{s}}\dot{\boldsymbol{\omega}} - \tilde{\boldsymbol{\omega}}\tilde{\mathbf{s}}\tilde{\mathbf{s}}\boldsymbol{\omega} \tag{A.32}$$

with $\boldsymbol{\omega} = [\omega_{(x)}, \omega_{(y)}, \omega_{(z)}]^T$ the global representation of the angular velocity vector.

In agreement with the second necessary condition for planar motion, the body shown in Figure A.3 that rotates only about the ζ-axis, has an angular velocity vector of which only the z-component may be non-zero, i.e.:

$$\boldsymbol{\omega} = [0, 0, \omega_{(z)}]^T \tag{A.33}$$

with $\omega_{(z)} = \dot{\phi}$ (see Figure A.3).

Consequently, the skew-symmetric matrix $\tilde{\boldsymbol{\omega}}$ in (A.32) is given by:

$$\tilde{\boldsymbol{\omega}} = \begin{bmatrix} 0 & -\dot{\phi} & 0 \\ \dot{\phi} & 0 & 0 \\ 0 & 0 & 0 \end{bmatrix} \tag{A.34}$$

The time derivative of expression (A.33) is

$$\dot{\boldsymbol{\omega}} = [0, 0, \dot{\omega}_{(z)}]^T \tag{A.35}$$

with $\dot{\omega}_{(z)} = \ddot{\phi}$.

Hence, by substituting expressions (A.33) - (A.35) into the right hand side of expression (A.32), and isolating the third component of the resultant vector, gives for planar motion:

$$s_{(x)}\ddot{s}_{(y)} - s_{(y)}\ddot{s}_{(x)} = \ddot{\phi}(s^2_{(x)} + s^2_{(y)}) \tag{A.36}$$

Since for planar motion, the ζ-axis is parallel to the z-axis (see Figure A.3), it follows that:

$$s_{(x)}\ddot{s}_{(y)} - s_{(y)}\ddot{s}_{(x)} = \ddot{\phi}(s^2_{(x)} + s^2_{(y)}) = \ddot{\phi}(s^2_{(\xi)} + s^2_{(\eta)}) \tag{A.37}$$

Substituting expression (A.37) into expression (A.29) finally gives

$$n_{(z)} = \ddot{\phi} \int_{vol} (s^2_{(\xi)} + s^2_{(\eta)})\, dm \tag{A.38}$$

The integral in expression (A.38):

$$j_{\zeta\zeta} = \int_{vol} (s^2_{(\xi)} + s^2_{(\eta)})\, dm \tag{A.39}$$

is called the mass moment of inertia of the body about the ζ-axis through C.

Finally substituting expression (A.39) into expression (A.38) gives the *planar rotational equation of motion*:

$$n_{(z)} = \ddot{\phi}\, j_{\zeta\zeta} \tag{A.40}$$

Note that the global representation of the angular velocity vector $\omega = [0,0,\dot{\phi}]^T$ is equal to the local representation of the angular velocity vector $\omega' = [0,0,\dot{\phi}]^T$.

Appendix B

B FLOWCHART OF THE OCAS TRAJECTORY-PLANNING METHODOLOGY

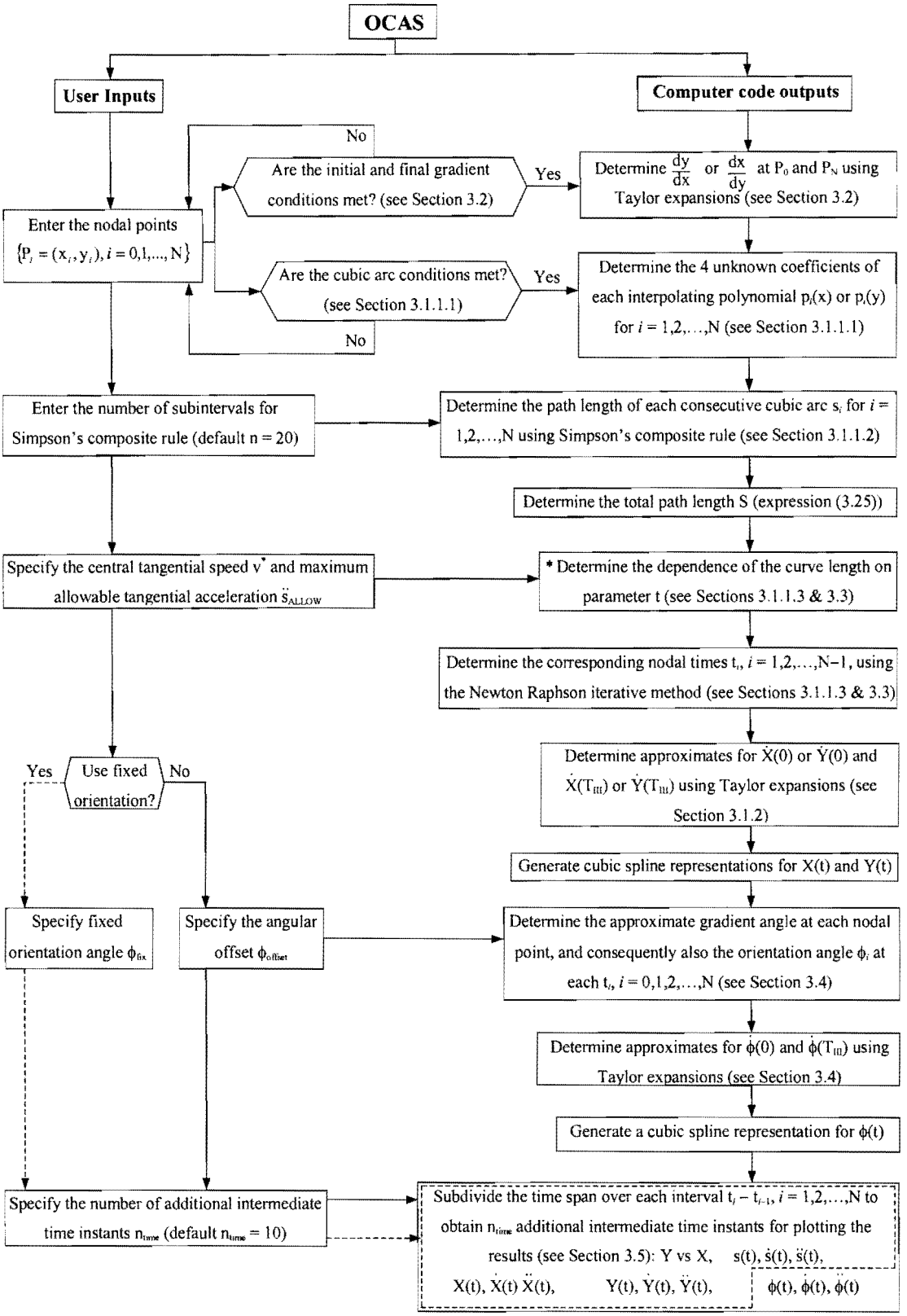

Figure B.1: OCAS flowchart.

* See detailed flowchart in Figure B.2

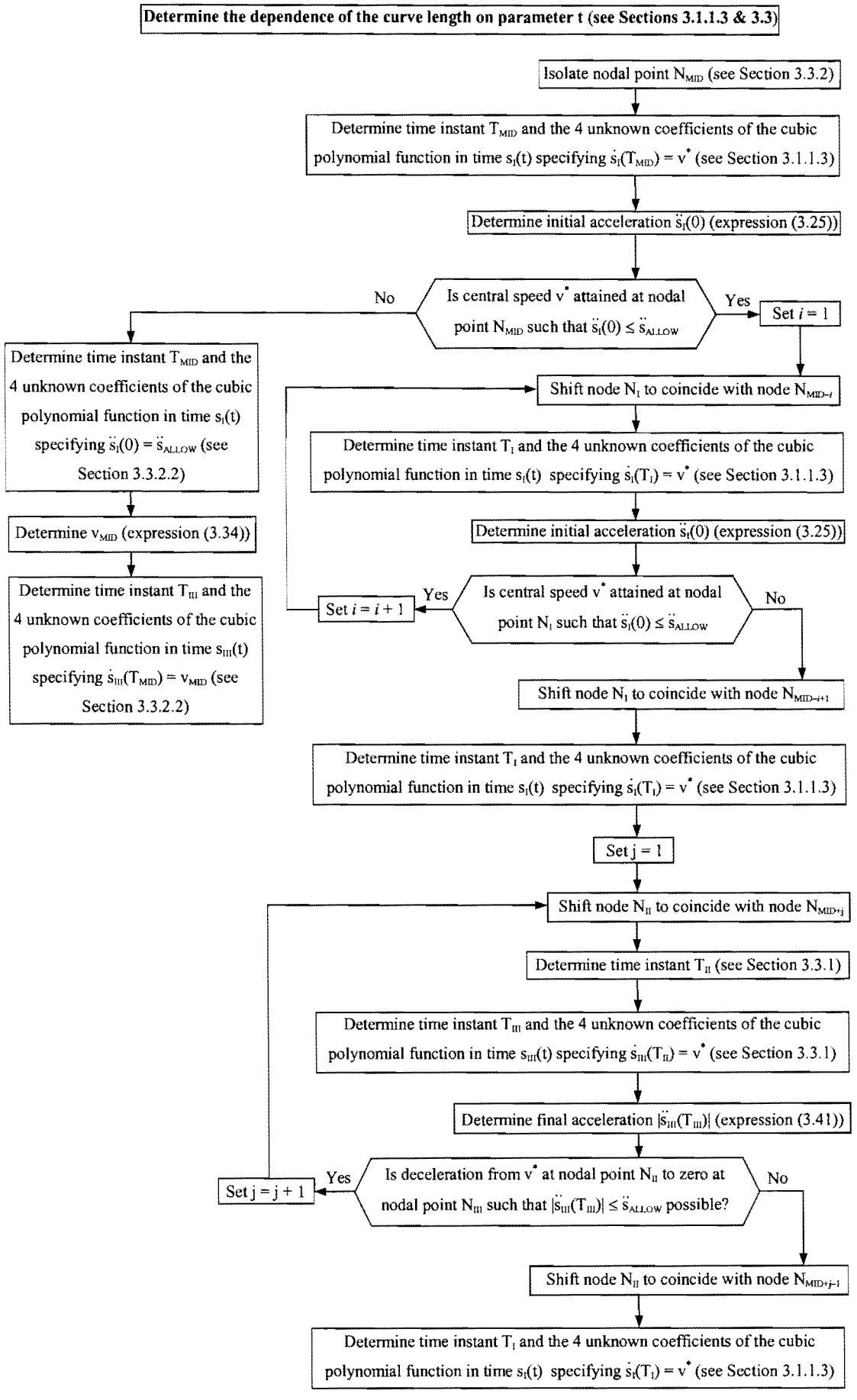

Figure B.2: Detail flowchart of determining the dependence of the curve length on t.

Appendix C

C THE LFOPC MATHEMATICAL OPTIMIZATION ALGORITHM

C.1 Background

The dynamic trajectory method (also called the "leap-frog" method) for the unconstrained minimization of a scalar function $F(\mathbf{X})$ of n real variables represented by the vector $\mathbf{X} = [X_1, X_2, ..., X_n]^T$ was originally proposed by Snyman [64, 74]. The original algorithm has recently been modified to handle constraints by means of a penalty function formulation. (Snyman et al [75, 76]). The method possesses the following characteristics:

- It uses only function *gradient* information $\nabla F(\mathbf{X})$.
- *No* explicit *line searches* are performed.
- It is extremely *robust* and handles steep valleys and discontinuities in functions and gradients with ease.
- The algorithm seeks *low local minimum* and can therefore be used as a basic component in a methodology for global optimization.
- The method is not as efficient as classical methods on smooth and near-quadratic functions.

C.2 Basic dynamic model

The algorithm is modeled on the motion of a particle of unit mass in a n-dimensional conservative force field with potential energy at $\mathbf{X}$ given by $F(\mathbf{X})$. At $\mathbf{X}$, the force on the particle is given by

$$\mathbf{a} = \ddot{\mathbf{X}} = -\nabla F(\mathbf{X}) \tag{C.1}$$

from which it follows that for the time interval $[0, t]$:

$$\begin{aligned} \tfrac{1}{2}\left\|\dot{\mathbf{X}}(t)\right\|^2 - \tfrac{1}{2}\left\|\mathbf{X}(0)\right\|^2 &= F(\mathbf{X}(0)) - F(\mathbf{X}(t)) \\ T(t) - T(0) &= F(0) - F(t) \end{aligned} \tag{C.2}$$

or

$$F(t) + T(t) = \text{constant } \{\text{conservation of energy}\}$$

Note that since $\Delta F = -\Delta T$ as long as T increases F decreases. This forms the basis of the dynamic algorithm.

C.3 LFOP: Basic algorithm for unconstrained problems

Given $F(\mathbf{X})$ and a starting point $\mathbf{X}(0) = \mathbf{X}^0$

- Compute the dynamic trajectory by solving the initial value problem (IVP)

$$\ddot{\mathbf{X}}(t) = -\nabla F(\mathbf{X}(t))$$
$$\dot{\mathbf{X}}(0) = \mathbf{0}, \quad \mathbf{X}(0) = \mathbf{X}^0 \tag{C.3}$$

- Monitor $\dot{\mathbf{X}}(t) = \mathbf{v}(t)$. Clearly as long as $T = \frac{1}{2}\|\mathbf{v}(t)\|^2$ increases $F(\mathbf{X}(t))$ decreases and descent follows as required
- When $\|\mathbf{v}(t)\|$ decreases apply some interfering strategy to extract energy and thereby increasing the likelihood of descent.
- In practice a numerical integration "leap-frog" scheme is used to integrate the IVP (C.3). Compute for $k = 0,1,2,...$ and time step Δt

$$\mathbf{X}^{k+1} = \mathbf{X}^k + \mathbf{v}^k \Delta t$$
$$\mathbf{v}^{k+1} = \mathbf{v}^k + \mathbf{a}^{k+1} \Delta t \tag{C.4}$$

  where $\mathbf{a}^k = -\nabla F(\mathbf{X}^k), \quad \mathbf{v}^0 = \frac{1}{2}\mathbf{a}^0 \Delta t$

- A typical interfering strategy is:

  If $\|\mathbf{v}^{k+1}\| \geq \|\mathbf{v}^k\|$ continue

  else

$$\text{set } \mathbf{v}^k = \frac{\mathbf{v}^{k+1} + \mathbf{v}^k}{4}, \quad \mathbf{x}^k = \frac{\mathbf{x}^{k+1} + \mathbf{x}^k}{2} \tag{C.5}$$

  compute new $\mathbf{v}^{k+1}$ and continue.

- Further heuristics are used to determine an initial Δt, to allow for magnification and reduction of Δt, and to control the step size.

C.4 LFOPC: Modification for constrained problems

Constrained optimization problems are solved by the application, in three phases, of LFOP to a penalty function formulation of the problem [64, 76]. Given a function $F(\mathbf{X})$, $\mathbf{X} \in \Re^n$ with equality constraints $H_i(\mathbf{X}) = 0$ $(i = 1,2,...,p < n)$ and inequality constraints $C_j(\mathbf{X}) \le 0$ $(j = 1,2,...,m)$ and penalty parameter $\mu >> 0$, the penalty function problem is to minimize

$$P(\mathbf{x},\mu) = F(\mathbf{X}) + \sum_{i=1}^{p} \mu H_i^2(\mathbf{X}) + \sum_{j=1}^{m} \beta_j C_j^2(\mathbf{X}) \qquad \text{(C.6)}$$

$$\text{where } \beta_j = \begin{cases} 0 \text{ if } G_j(\mathbf{X}) \le 0 \\ \mu \text{ if } G_j(\mathbf{X}) > 0 \end{cases}$$

Phase 0: Given some $\mathbf{X}^0$, then with the overall penalty parameter $\mu = \mu_0 (= 10^2)$ apply LFOP to $P(\mathbf{X},\mu_0)$ to give $\mathbf{X}^*(\mu_0)$

Phase 1: With $\mathbf{X}^0 = \mathbf{X}^*(\mu_0)$, $\mu = \mu_1 (= 10^4)$ apply LFOP to $P(\mathbf{X},\mu_1)$ to give $\mathbf{X}^*(\mu_1)$ and identify active constraints $i_a = 1,2,...,n_a$; $g_{i_a}\left(\mathbf{X}^*(\mu_1)\right) > 0$

Phase 2: With $\mathbf{X}^0 = \mathbf{X}^*(\mu_1)$, use LFOP to minimize

$$P_a(\mathbf{X},\mu_1) = \sum_{i=1}^{p} \mu_1 H_i^2(\mathbf{X}) + \sum_{i_a=1}^{n_a} \mu_1 g_{i_a}^2(\mathbf{X}) \qquad \text{(C.7)}$$

to give $\mathbf{X}^*$.

Appendix D

D PHYSICAL SPECIFICATION FOR SIMULATION AND OPERATIONAL CONSTRAINTS OF THE TEST-MODEL

D.1 Introduction

This Appendix describes the physical specifications required for simulation of the motion of the test-model. In addition it deals in detail with the incorporation of further physical constraints to prevent mechanical interference during the operation of the test-model.

D.2 Physical specifications for simulation of the test-model

A photograph of the test-model is shown in Figure D.1. Figure D.2 is a scaled two-dimensional view of the test-model where the eight bodies comprising the mechanical system are numbered in accordance with Figure 2.5.

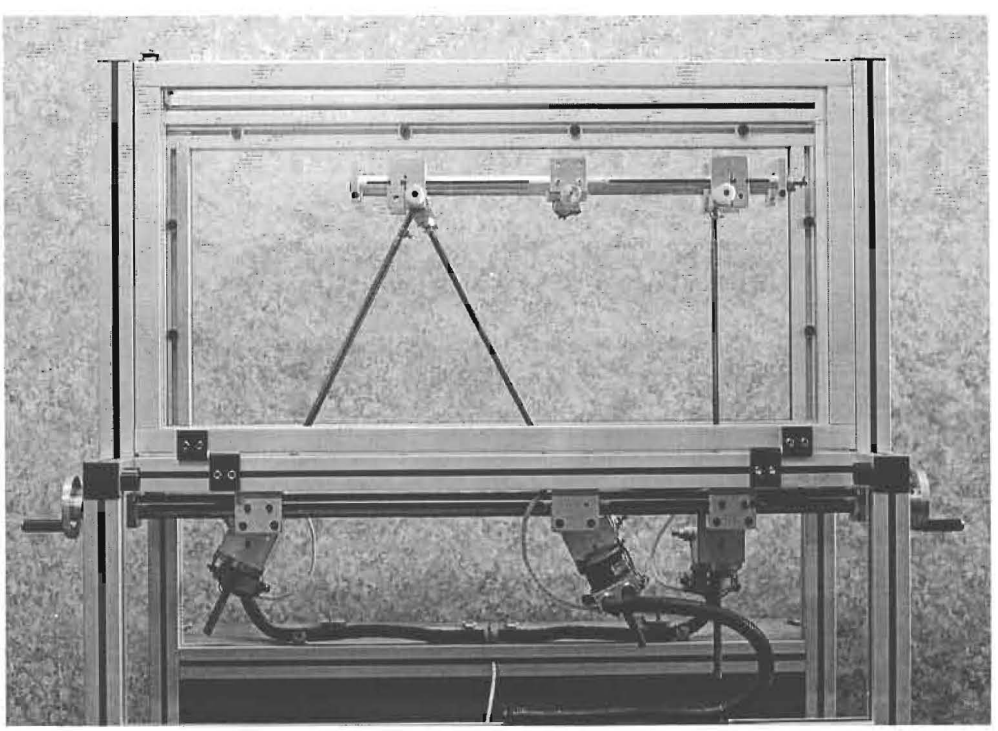

Figure D.1: Photograph of the test-model

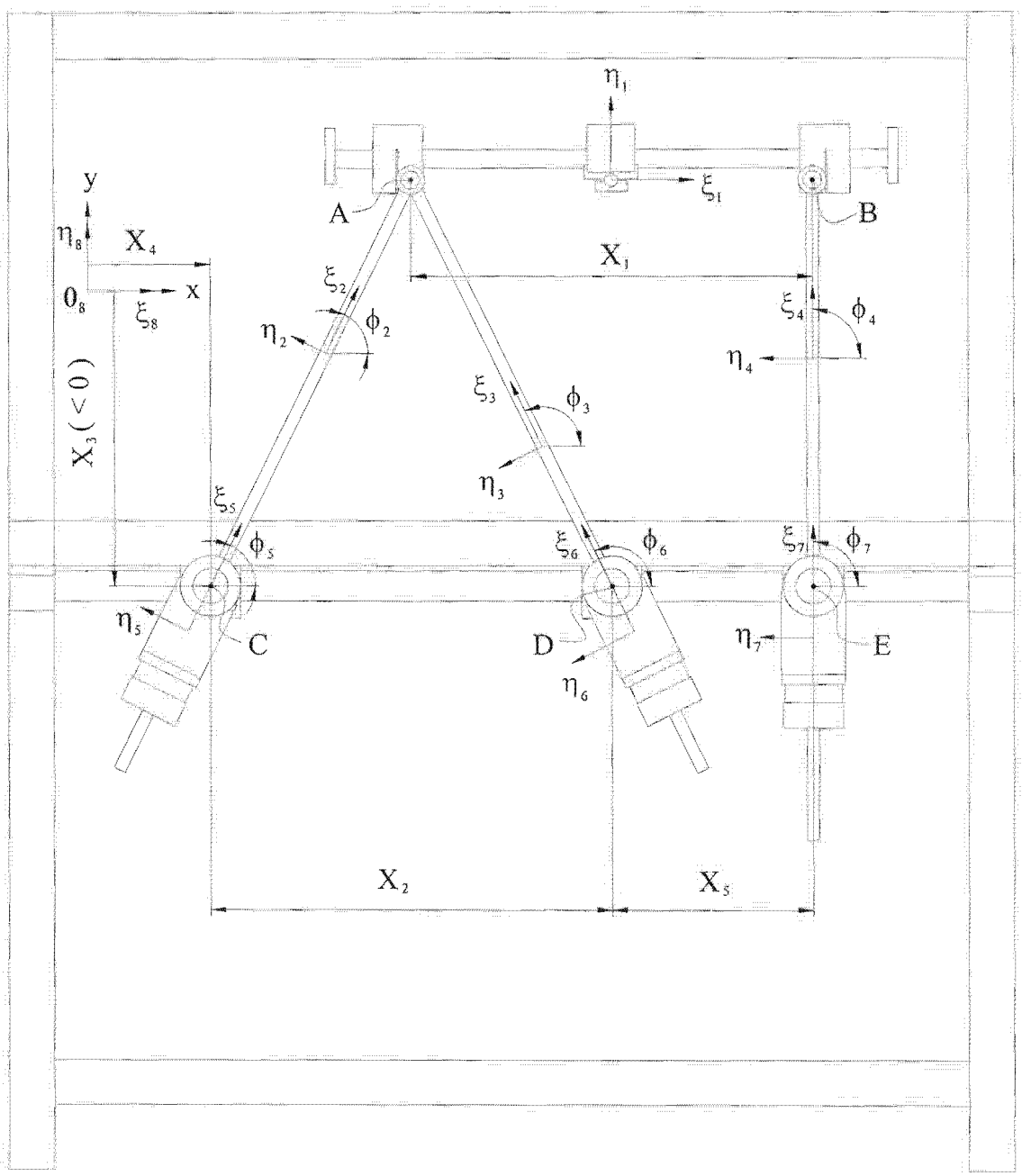

Figure D.2: Geometrical representation of the test-model as a mechanical system of eight bodies.

D.2.1 Operational geometry

Note that the same five design variables $\mathbf{X} = [X_1, X_2, X_3, X_4, X_5]^T$, introduced in Section 4.2.1, are used here to describe the adjustable operational geometry of the physical test-model.

Design variable X_1 indicates the distance between revolute joints A and B on the moving platform. The center of mass of the moving platform is taken as midway between revolute joints A and B, hence $\xi_1^A = -\frac{X_1}{2}$ and $\xi_1^B = \frac{X_1}{2}$.

Note that the absolute position of revolute joint D on the base twin tubular rails is fixed. Design variables X_2, X_3 and X_4 therefore determine the relative position of the global $0xy$-coordinate system, relative to the positionally fixed revolute joint D. More specifically, $x = 0$ is at $-|X_2| - X_4$ relative to revolute joint D, and $y = 0$ is at $-X_3$ relative to revolute joint D.

For the fixed workpiece case of Section 2.4.1 and 2.6.4.2.1, the prescribed tool path is specified in terms of the global $0xy$- coordinate system. Hence, a change in design variables X_2, X_3 and X_4 will shift the position of the prescribed tool path relative to revolute joint D.

The use of the test-model is currently limited to the execution of prescribed paths specified in the fixed workpiece. With an extension of the test-model capabilities, it would also be possible to demonstrate the machining operation for the fixed tool scenario as explained in Sections 2.4.2 and 2.6.4.2.2.

For the fixed tool case, the fixed tool tip traces the prescribed tool path specified in terms of local $0_1\xi_1\eta_1$-coordinate system, and a change in design variables X_2, X_3 and X_4 will vary the position of the fixed tool tip relative to revolute joint D.

Finally design variable X_5 indicates the relative distance between revolute joints D and E, so that for simulation purposes, the global positions of revolute joints C, D and E are given by expression (4.3): $(x,y)_C = (X_4, X_3)$, $(x,y)_D = ((X_4 + X_2),(X_3))$ and $(x,y)_E = ((X_4 + X_2 + X_5),(X_3))$.

D.2.2 Local coordinates

Given a prescribed tool path, as well as an operational geometry $\mathbf{X} = [X_1, X_2, X_3, X_4, X_5]^T$, the physical motion of the test-model platform may be simulated to find the overall maximum magnitudes along the path of the individual actuator forces f_k, $k = 1,2,3$. This objective function (expression (4.4)) is formally defined in Section 4.2.2.

In evaluating the objective function (see Section 4.3.1), the inverse kinematic analysis of the test-model requires that the global coordinates of revolute joints C, D and E, as well as the local coordinates ξ_1^A,

ξ_1^B, ξ_2^A, ξ_3^A, ξ_4^B, ξ_5^C, ξ_6^D and ξ_7^E be known. The global coordinates of revolute joints C, D and E are given by substituting the specific values of the relevant design variables into expression (4.3) (see also the last paragraph of Section D.2.1). The value of design variable X_1 fixes the values of local coordinates ξ_1^A and ξ_1^B as explained in the second paragraph of Section D.2.1.

Corresponding to Section 2.3, the origin of each local $0_i\xi_i\eta_i$-coordinate system, $i = 1,2,...,7$ is chosen to coincide with the center of mass of respective bodies $1,2,...,7$. Using the known dimensions and densities of the components that make up each individual body of the test-model, the positions of each body's center of mass may be calculated. With reference to Figure D.2, the following local coordinates of the test-model are fixed:

$$\begin{aligned} \xi_2^A &= 0.1904\,\text{m} & \xi_3^A &= 0.2921\,\text{m} & \xi_4^B &= 0.1751\,\text{m} \\ \xi_5^C &= 0.050\,\text{m} & \xi_6^D &= 0.050\,\text{m} & \xi_7^E &= 0.050\,\text{m} \end{aligned} \tag{D.1}$$

The evaluation of the objective function, furthermore involves solving the inverse dynamic equations of motion (expression (2.124)) for the unknown LaGrange multipliers and actuator forces **ff** (see Section 4.3.1).

D.2.3 Gravitational and frictional external forces

The specific entries of the constant diagonal mass matrix **M** in expression (2.124) consist of the specific masses and moments of inertia of the individual bodies of the test-model (see **Chapter 5**), and may also be determined using the known dimensions and densities of the parts constituting each body. With reference to the eight numbered bodies of Figure D.2, the entries of the mass matrix **M** are

$$\mathbf{M} = \text{diag}[\mathbf{M}_1^T, \mathbf{M}_2^T, ..., \mathbf{M}_8^T] \tag{D.2}$$

with

$$\mathbf{M}_1 = [2.1246, 2.1246, 0.0829]^T$$

$$\mathbf{M}_2 = [0.7671, 0.7671, 0.0355]^T$$

$$\mathbf{M}_3 = [0.5696, 0.5696, 0.0263]^T$$

$$\mathbf{M}_4 = [0.8341, 0.8341, 0.0377]^T$$

$$\mathbf{M}_5 = \mathbf{M}_6 = \mathbf{M}_7 = [3.0725, 3.0725, 6.17 \times 10^{-3}]^T$$

$$\mathbf{M}_8 = [0, 0, 0]^T$$

and specified in SI units.

The vector of known external forces $\mathbf{g}^{(k)}$ in expression (2.124) consists of the cutting force $\mathbf{g}_1^{(\text{cutting f})}$ acting on the moving platform (body 1) and the weights of individual bodies comprising the planar Gough-Stewart platform $\mathbf{g}_i^{(\text{gravity})}$, $i = 1,2,...,7$ (see expression (2.124)).

With the masses of the individual bodies of the platform test-model known (see **Chapter 5**), their respective weights follow from expression (2.104), i.e.:

$$\mathbf{g}_1^{(\text{gravity})} = [0, -20.842\,\text{N}, 0]^T$$

$$\mathbf{g}_2^{(\text{gravity})} = [0, -7.526\,\text{N}, 0]^T$$

$$\mathbf{g}_3^{(\text{gravity})} = [0, -5.588\,\text{N}, 0]^T$$

$$\mathbf{g}_4^{(\text{gravity})} = [0, -8.182\,\text{N}, 0]^T$$

$$\mathbf{g}_5^{(\text{gravity})} = \mathbf{g}_6^{(\text{gravity})} = \mathbf{g}_7^{(\text{gravity})} = [0, -30.141\,\text{N}, 0]^T$$

The platform test-model represents a special case of the fixed work-piece scenario, with a zero tool length $\eta_1^P = 0$ (see Section 2.4.1). This is because the pen, used for demonstration purposes, is mounted on the moving platform (body 1) at local coordinates $(\xi, \eta)_1 = (0, 0)$.

The cutting force $\mathbf{g}_1^{(\text{cutting f})}$ of the fixed workpiece case is described in Section 2.6.4.2.1. Note that the cutting force is modeled as a friction force, the magnitude of which is linearly dependent on the magnitude of the cutting velocity (see expression (2.107)). The moving platform of the test-model experiences frictional forces, not only as a result of the pen tracing the prescribed tool path on the Perspex side panel, but also because of the spring loaded lateral stiffeners (see **Chapter 5**) sliding against the Perspex side panels during the motion of the moving platform.

The magnitude of the resultant frictional force may be measured by means of a simple experiment using a spring balance. In particular, the moving platform is disconnected from the three actuator legs, and hung unto a string. The experiment is executed by connecting the moving platform to the spring balance, and pulling the moving platform in a horizontal direction while the pen and spring loaded lateral stiffeners slide against the Perspex side panels. While moving at a constant speed along a known distance, the "constant speed motion" time and spring balance reading are measured.

Since the string supporting the moving platform is very long (1.38 m) compared to the horizontal motion (80 mm) of the moving platform, the vertical displacement of the moving platform may be neglected, hence the reading on the spring balance approximately equals the resultant frictional force.

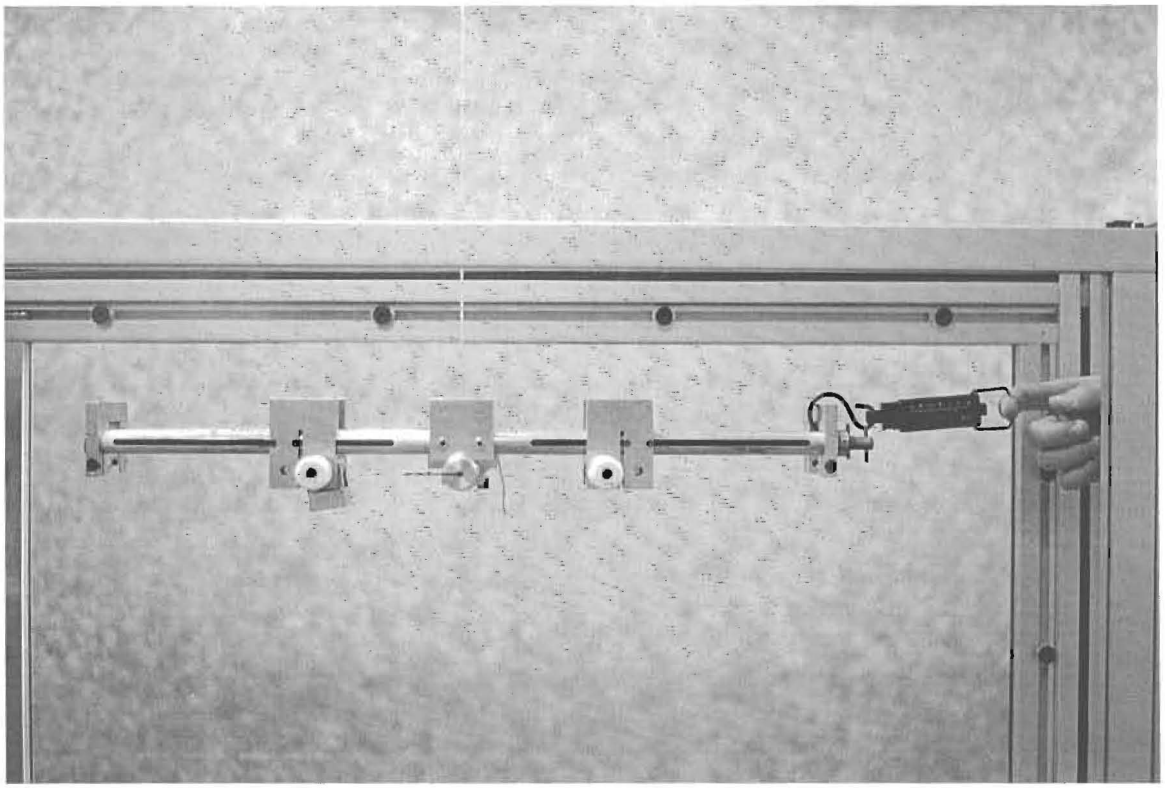

Figure D.3: The experimental setup for measuring the frictional force using a spring balance.

Figure D.3 shows a photograph of the experimental setup used to measure the resultant frictional force on the moving platform using the spring balance. Table D.1 lists the readings that were obtained, as well as the calculation of the average cutting force constant, C_{cut}. The reasonable assumption is made here that the friction forces acting on the moving platform may be merged and simulated as a single cutting force (see Section 2.6.4.2.1). In order to determine the average cutting force constant, C_{cut} used in expression (2.107), the experimental constant speed translations listed in Table D.1 were also measured and timed to yield the magnitudes of the constant speeds.

Spring balance reading No.	**Resultant friction force** [N]	**Distance** [mm]	**Time** [s]	**Constant speed** [m/s]	C_{cut} [Ns/m]
1	7.85	80 mm	3.74	0.02139	366.894
2	9.81	80 mm	1.54	0.05195	188.843
3	11.28	80 mm	1.13	0.07080	159.351
4	8.34	80 mm	3.57	0.02241	372.106
5	9.81	80 mm	1.23	0.06504	150.829
6	10.3	80 mm	1.39	0.05755	178.971
7	11.77	80 mm	0.77	0.10390	113.306
8	8.34	80 mm	3.17	0.02524	330.413

9	9.81	80 mm	1.42	0.056338	174.128
10	11.28	80 mm	1.39	0.05755	196.016
11	10.79	80 mm	1.17	0.06838	157.818
12	7.85	80 mm	3.43	0.02332	336.483
13	8.83	80 mm	4.16	0.01923	459.108
14	19.81	80 mm	1.58	0.05063	193.748
15	8.34	80 mm	4.89	0.01636	509.691
16	9.81	80 mm	1.71	0.04678	209.689
17	11.28	80 mm	1.01	0.07921	142.429
				Average	249.4

Table D.1: Experimental readings in determining the average "cutting force constant".

The average value for C_{cut} as determined from the experimental measurements is 249.4 . The specific value used in all for the simulations of the motion of the platform test-model, is 250.

D.3 Specification of the physical operational constraints of the test-model

In illustrating the optimization methodology, the configurational constraints (expressions (4.5) and (4.6)), relating to dimensional limitations of the individual components of the manipulator, were the only inequality constraints specified to ensure a feasible design for the *hypothetical* planar machining center. For the *real* test-model some of the physical limitations of the planar mechanism may also be incorporated in these configurational constraints, while others, specifically those relating to the prevention of *mechanical interference*, must be dealt with separately.

In this section, the latter constraints are first explained in general terms below, followed by a categorization of the test-model physical limitations, and an explanation of the necessary inequality constraints with which a feasible test-model design may be obtained.

D.3.1 Inequality constraint specification for the prevention of mechanical interference

In general the instantaneous perpendicular distance between a line in body j and a point in body *i* may easily be determined for the special case where the line is parallel to the ξ-axis of body j.

Consider for example Figure D.4 showing the schematic representation of bodies *i* and j experiencing planar motion.

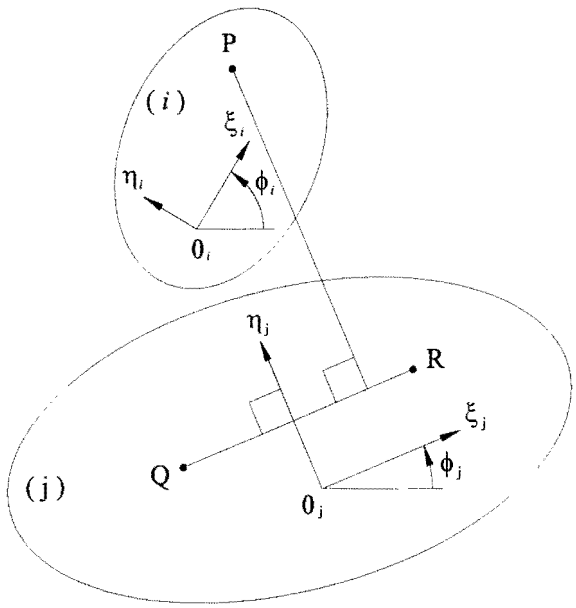

Figure D.4: Schematic representation of bodies *i* and j experiencing planar motion.

It is assumed here that the following are known:

1. the *instantaneous* positions and orientations of respective bodies *i*, $\mathbf{q}_i = [\mathbf{r}^T, \phi]_i^T = [x, y, \phi]_i^T$, and j, $\mathbf{q}_j = [\mathbf{r}^T, \phi]_j^T = [x, y, \phi]_j^T$, as defined by expression (2.2).
2. the *fixed* local coordinates of point P in body *i*, $(\xi^P, \eta^P)_i$, and
3. the *fixed* local η-coordinate of line QR in body j, η_j^{QR}

Using the transformation given by expression (2.1), the *instantaneous* global x- and y coordinates of point P may be determined, i.e.,

$$\begin{aligned} x^P &= x_i + \xi_i^P \cos\phi_i - \eta_i^P \sin\phi_i \\ y^P &= y_i + \xi_i^P \sin\phi_i + \eta_i^P \cos\phi_i \end{aligned} \tag{D.3}$$

The *instantaneous* η-coordinate of point P relative to the local coordinate system of body j, η_j^P, may also be determined using the *inverse* of the transformation given by expression (2.1), i.e.,

$$\mathbf{s}_j'^P = \mathbf{A}_j^{-1} \mathbf{s}_j^P \tag{D.4}$$

with $\mathbf{A}_j^{-1} = \begin{bmatrix} \cos\phi_j & \sin\phi_j \\ -\sin\phi_j & \cos\phi_j \end{bmatrix}$.

Substituting $\mathbf{s}_j^P = \mathbf{r}_j^P - \mathbf{r}_j$ (see expression (2.1)) into expression (D.4), yields

$$\begin{bmatrix} \xi^P \\ \eta^P \end{bmatrix}_j = \begin{bmatrix} \cos\phi_j & \sin\phi_j \\ -\sin\phi_j & \cos\phi_j \end{bmatrix} \begin{bmatrix} x^P - x_j \\ y^P - y_j \end{bmatrix}$$

and therefore

$$\eta_j^P = (y^P - y_j)\cos\phi_j - (x^P - x_j)\sin\phi_j \qquad \text{(D.5)}$$

Hence, the instantaneous perpendicular distance between line QR and point P is given by

$$\delta_{P-QR} = \eta_j^P - \eta_j^{QR} \qquad \text{(D.6)}$$

Note that for the relative positioning of bodies *i* and j shown in Figure D.4, δ_{P-QR} will become *smaller* as the two bodies move closer to each other. Hence, if the two bodies shown in Figure D.4 move relative to each other over a time interval $[0,T] = [0,T_{Mtime}]$, the instantaneous perpendicular distance δ_{P-QR} (expression (D.6)) may be monitored at discrete time instants t_j to find the *overall minimum* perpendicular distance, i.e. $\delta_{P-QR}^{min} = \min_j[\delta_{P-QR}(t_j)]$ for $t_j = j\Delta t$; $j = 0,1,2,...,M_{time}$; where $M_{time} = \dfrac{T}{\Delta t}$ and Δt is a suitably small chosen *monitoring* time interval.

The alternative relative positioning of bodies *i* and j is shown in Figure D.5. Here the instantaneous perpendicular distance δ_{P-QR} (expression (D.6)) becomes *larger* as the two bodies move closer to each other. Hence, if the two bodies shown in Figure D.5 move relative to each other over a time interval $[0,T] = [0,T_{Mtime}]$, the instantaneous perpendicular distance δ_{P-QR} (expression (D.6)) may be monitored at discrete time instants t_j to find the *overall maximum* perpendicular distance, i.e. $\delta_{P-QR}^{max} = \max_j[\delta_{P-QR}(t_j)]$ for t_j as defined above.

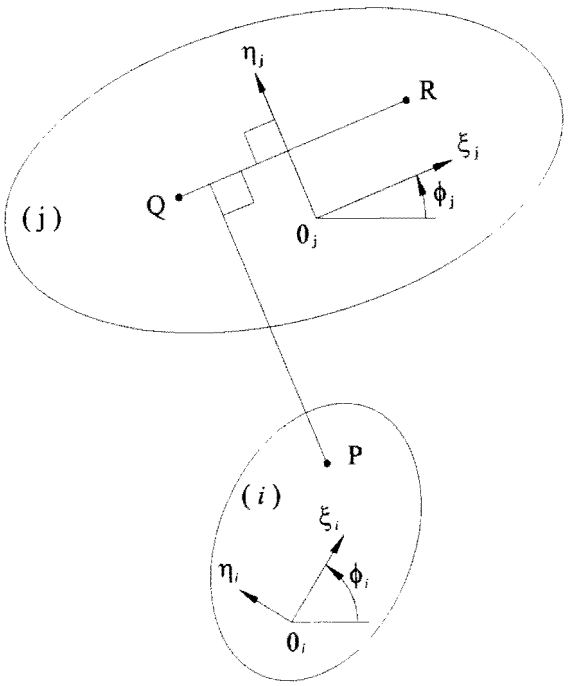

Figure D.5: Schematic representation of bodies *i* and j experiencing planar motion (alternative relative positioning of the two bodies).

With the judicious selection of point P on body *i*, and points Q and R on body j, mechanical interference between bodies *i* and j may be prohibited for both situations as depicted in Figure D.4 and Figure D.5 respectively: Firstly, an *allowable* perpendicular distance $\left|\delta_{P-QR}^{allow}\right|$ is chosen. Secondly, one of the following two inequality constraints is specified:

$$\left|\delta_{P-QR}^{allow}\right| \leq \delta_{P-QR}^{min} \tag{D.7}$$

or

$$\delta_{P-QR}^{max} \leq -\left|\delta_{P-QR}^{allow}\right| \tag{D.8}$$

Inequality constraint (D.7) is used for the relative positioning of bodies *i* and j as shown in Figure D.4, while inequality constraint (D.8) is used for the relative positioning of bodies *i* and j as shown in Figure D.5.

D.3.2 Linearly adjustable revolute joints

The configurational constraints limiting the allowable relative distances between the linearly adjustable revolute joints of the fixed base (X_2 and X_5) and the moving platform (X_1) (see expression (4.5)) are directly applicable on the physical test-model. With reverence to Figure D.6 showing the adjustable capability of the test-model, the specific bounds (given in meters) on design variables X_1, X_2 and X_5 are

$$\begin{aligned} 0.1 \le X_1 \le 0.45 \\ 0.113 \le X_2 \le 0.465 \\ 0.113 \le X_5 \le 0.27 \end{aligned} \qquad \text{(D.9)}$$

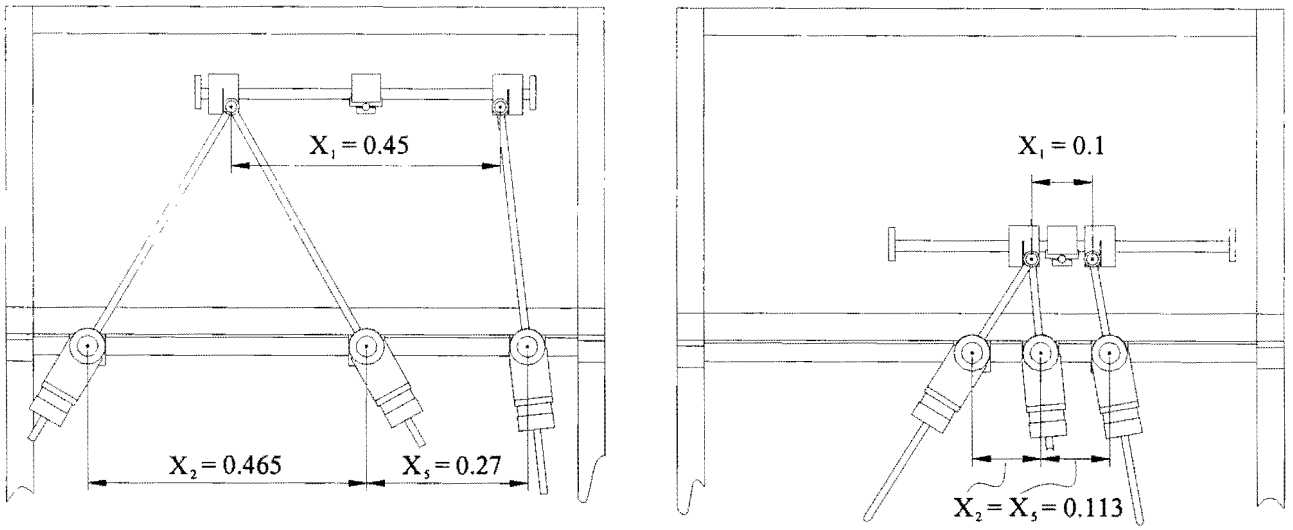

Figure D.6: Adjustable capability of the test-model.

The lower and upper bounds specified in expression (D.9) correspond exactly to the lower and upper bounds that were specified for the optimization test run of the hypothetical planar machining center (see expression (4.14)). Hence, in agreement with the inequality constraints given by expression (4.7), the first six inequality constraints used to ensure a feasible test-model design, are

$$\begin{aligned} C_1(\mathbf{X}) \equiv X_1 - 0.45 \le 0 \\ C_2(\mathbf{X}) \equiv 0.1 - X_1 \le 0 \\ C_3(\mathbf{X}) \equiv X_2 - 0.465 \le 0 \\ C_4(\mathbf{X}) \equiv 0.113 - X_2 \le 0 \\ C_5(\mathbf{X}) \equiv X_5 - 0.27 \le 0 \\ C_6(\mathbf{X}) \equiv 0.113 - X_5 \le 0 \end{aligned} \qquad \text{(D.10)}$$

D.3.3 Extreme motion constraints

The extreme motion of the hypothetical moving platform is bounded by the *allowable* minimum and maximum actuator leg lengths (see expressions (4.6) and (4.8)). On the other hand, the motion of the physical moving platform is to be confined within the four frame boundaries represented by the four sides of rectangle FGHI as annotated in Figure D.7.

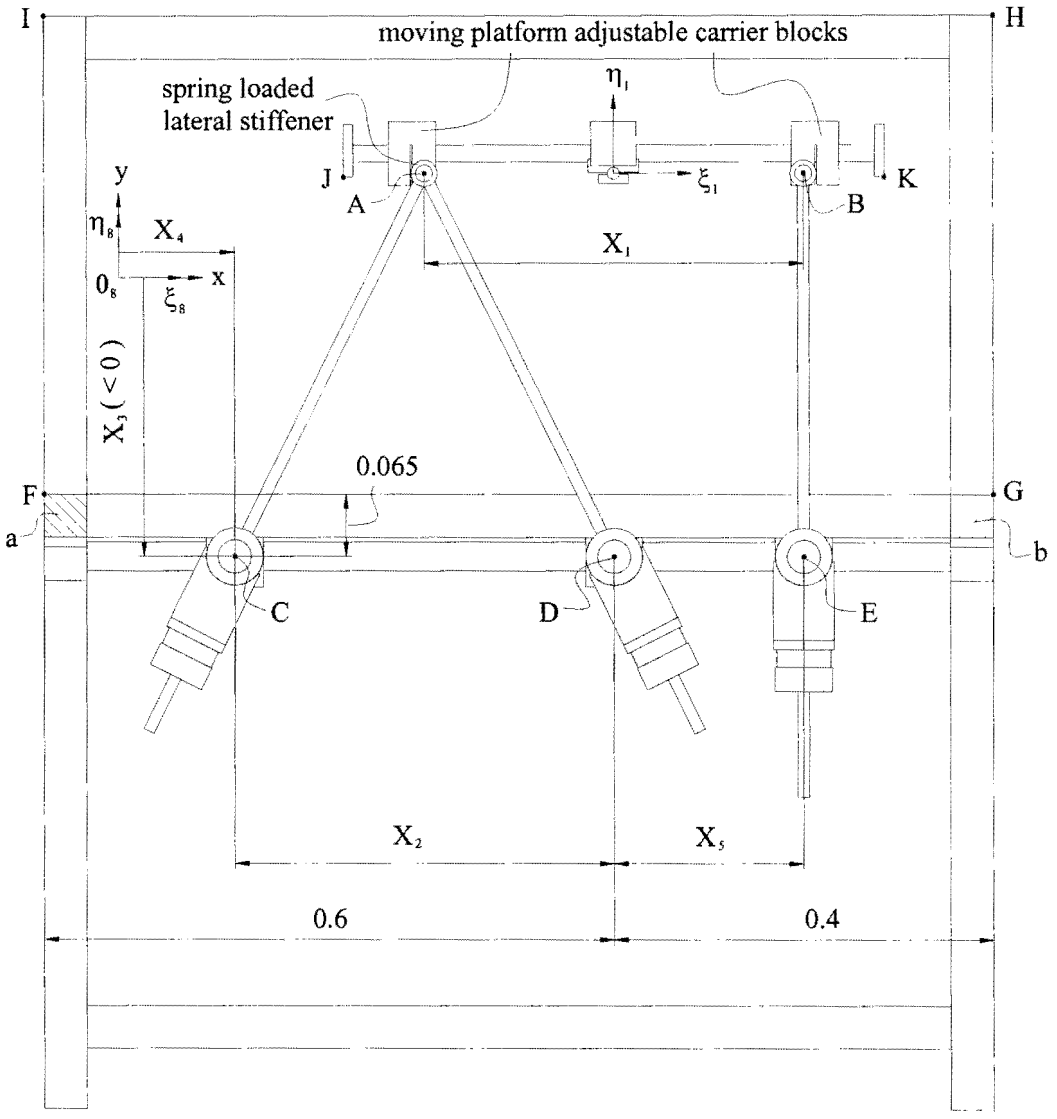

Figure D.7: Frame boundaries FGHI.

D.3.3.1 Upper frame boundary

The *upper frame boundary* (line HI) cannot be exceeded by the lateral stiffeners on the moving platform with specification that the *allowable* maximum actuator leg length $\bar{\ell}_k$ for all three actuator legs $k = 1,2,3$ is 0.525 m. Figure D.8 serves to illustrate this fact.

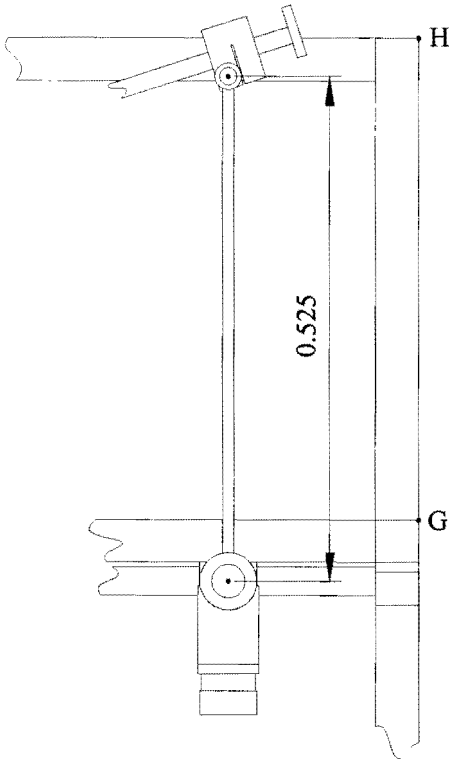

Figure D.8: Scaled two-dimensional view of an actuator leg extended to its maximum allowable leg length.

Test-model inequality constraints 7-9 are given by

$$C_7(\mathbf{X}) \equiv \ell_1^{max}(\mathbf{X}) - 0.525 \leq 0$$
$$C_8(\mathbf{X}) \equiv \ell_2^{max}(\mathbf{X}) - 0.525 \leq 0 \qquad \text{(D.11)}$$
$$C_9(\mathbf{X}) \equiv \ell_3^{max}(\mathbf{X}) - 0.525 \leq 0$$

where the overall maximum leg lengths for any prescribed path are given by $\ell_k^{max}(\mathbf{X})$, $k = 1,2,3$ as explained in Section 4.3.2. These constraints (expression (4.8)) correspond exactly to the constraints $C_{k+6}(\mathbf{X}) \equiv \ell_k^{max}(\mathbf{X}) - 0.525 \leq 0$, $k = 1,2,3$ specified for the optimization of the hypothetical platform see expression (4.8).

D.3.3.2 Lower frame boundary

The *lower frame boundary* of the test-model is represented by line FG in Figure D.7. Here it is important to prevent mechanical interference between the moving platform and the bottom frame cross members indicated by shaded regions a and b in Figure D.7. Line FG coincides with the top plane of the two bottom frame cross members.

With the moving platform in a horizontal orientation, the bottom ends of the adjustable brackets of revolute joints A and B are the lowest points on the moving platform (see Figure D.7). Due to the fact that the relative positions of the revolute joints may be adjusted, it is highly unlikely that the adjustable

brackets of revolute joints A and B will collide with the bottom frame cross members (shaded regions a and b), even with the moving platform in a horizontal orientation ($\phi_1 = 0$). Furthermore, for a large enough CCW rotation of the moving platform, point J indicated in Figure D.7 is the lowest point on the moving platform. Similarly, for a large enough CW rotation of the moving platform, point K (see Figure D.7) is the lowest point on the moving platform.

The lower frame boundary is therefore treated here by monitoring the perpendicular distances between line FG on the frame, and respective points J and K on the moving platform following the methodology explained in Section D.3.1. In particular, assumptions 1 - 3 listed in Section D.3.1 are valid here, since the instantaneous position (x_1, y_1) and orientation ϕ_1 of the moving platform (body 1 in Figure D.2) are known as the prescribed path is traced (see expressions (2.27) – (2.29)). Furthermore, the global position (x_8, y_8) and orientation ϕ_8 of the frame (body 8 in Figure D.2) are fixed: $[x_8, y_8, \phi_8]^T = [0,0,0]^T$. The fixed local coordinates (in meters) of points J and K are $(\xi^J, \eta^J)_1 = (-0.285, -0.004)$ and $(\xi^K, \eta^K)_1 = (0.285, -0.004)$, and the fixed local η-coordinate of line FG is $\eta_8^{FG} = X_3 + 0.065$. Note that X_3 is the design variable representing the y-coordinate of the three base revolute joints C, D and E (see Figure D.2). Hence, the respective instantaneous perpendicular distances $\delta_{J-FG}(\mathbf{X}, t_{i,j})$ and $\delta_{K-FG}(\mathbf{X}, t_{i,j})$ may be determined at any time instant $t_{i,j}$, $i = 0,1,2,\ldots,N-1$, $j = 0,1,2,\ldots,n_{time}$ (see Section 4.2.2) in accordance with expressions (D.3) - (D.6). The default value for $n_{time} = 10$ (see **Appendix B**).

Since the relative positioning of the moving platform with respect to the lower frame boundary conforms to the relative positioning of the bodies i and j as depicted in Figure D.4, the *lower frame boundary inequality constraints* formulated here correspond to the inequality (D.7):

$$\begin{aligned} C_{10}(\mathbf{X}) &\equiv 0.006 - \delta_{J-FG}^{min}(\mathbf{X}) \leq 0 \\ C_{11}(\mathbf{X}) &\equiv 0.006 - \delta_{K-FG}^{min}(\mathbf{X}) \leq 0 \end{aligned} \qquad \text{(D.12)}$$

where $\delta_{J-FG}^{min}(\mathbf{X}) = \min_{i,j}[\delta_{J-FG}(\mathbf{X}, t_i + t_j)]$, and $\delta_{K-FG}^{min}(\mathbf{X}) = \min_{i,j}[\delta_{K-FG}(\mathbf{X}, t_i + t_j)]$, and with t_i and t_j as defined above.

The same value of 0.006 m is used for both allowable perpendicular distances $|\delta_{J-FG}^{allow}|$ and $|\delta_{K-FG}^{allow}|$ in expression (D.12). This value was chosen, so that the shortest attainable actuator leg length, without violating inequality constraints C_{10} and C_{11} (expression (D.12)), is 0.075 m as shown in Figure D.9. This length is also the *allowable* minimum actuator leg length specified for the hypothetical platform in expression (4.15).

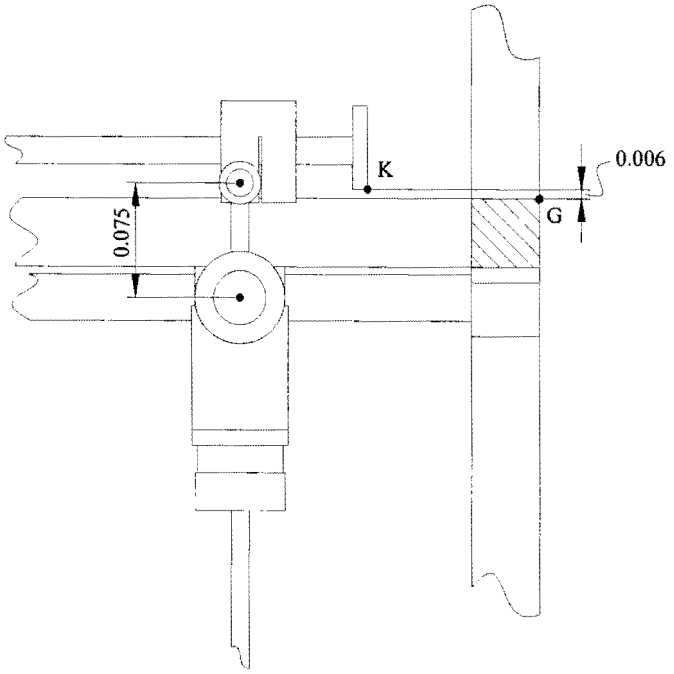

Figure D.9: Shortest attainable actuator leg length.

Since the shortest attainable actuator leg length corresponds exactly to the allowable minimum actuator leg length, inequality constraints $C_{k+9}(\mathbf{X}) \equiv \underline{\ell}_k - \ell_k^{\min}(\mathbf{X}) \leq 0$, $k = 1,2,3$ (expression (4.8)) specified for the hypothetical platform are redundant in the optimization of the platform test-model.

D.3.3.3 Left hand frame boundary

The *left-* and *right hand frame boundaries* limit the horizontal movement of the physical moving platform. With the use of the spring loaded lateral stiffeners (see **Chapter 5**), point A is restricted to the right hand side of line FI, and point B is restricted to the left hand side of line GH (see Figure D.7).

Consider for the moment the left hand frame boundary. Point A is on the moving platform (body 1 in Figure D.2) at local coordinates $(\xi^A, \eta^A)_1 = \left(-\frac{X_1}{2}, 0\right)$, and the global position and orientation of body 1 $[x_1, y_1, \phi_1]^T$ are known at each time instant as the prescribed path is traced. The global position of point A may therefore be determined in accordance with expression (D.3).

Line FI on the frame (body 8 in Figure D.2) is dealt with in a special manner. According to the definitions given in Section 2.3, the fixed body 8 is considered as the *ground* of the planar Gough-Stewart platform mechanism. Figure D.2 shows that the origin of body 8 is chosen to coincide with the origin of the global $0xy$-reference frame, $(x_8, y_8) = (0,0)$, and that the local $0_8\xi_8\eta_8$-coordinate system and the global $0xy$-reference frame are identically orientated, i.e. $\phi_8 = 0$. This implies that the fixed

vertical line FI is parallel to the η-axis of body 8. However, the proposed collision prevention methodology explained in Section D.3.1 is based on the assumption that the line in body j is parallel to the ξ-axis of body j (see Figure D.4). The special treatment of line FI consists of the specification that body 8 is angled at 90°, i.e. $\phi_8 = \frac{\pi}{2}$ rad, and is allowable, since each inequality constraint is treated separately and independent of the kinematic and kinetic analysis (**Chapter 2**).

The global x-coordinate of line FI is $x^{FI} = X_4 + X_2 - 0.6$ (see Figure D.7), with X_4 and X_2 two of the five design variables describing the adjustable geometry of the planar Gough-Stewart platform machining center (see Figure 4.1). With the specification that $[x_8, y_8, \phi_8]^T = \left[0,0,\frac{\pi}{2}\right]^T$, the local η-coordinate of line FI may be determined using the transformation given by expression (D.4): $\eta_8^{FI} = -(X_4 + X_2 - 0.6)$.

The instantaneous perpendicular distance between point A on the moving platform and line FI on the frame δ_{A-FI} may therefore be determined in accordance with expression (D.6). The relative positioning of the moving platform with respect to the left hand frame boundary agrees with the relative positioning of bodies *i* and j as depicted in Figure D.5. As a result of this, the instantaneous perpendicular distance δ_{A-FI} becomes *larger* as the moving platform moves closer to the left hand frame boundary. The *left hand frame boundary inequality constraint* is therefore given by

$$C_{12}(\mathbf{X}) \equiv \delta_{A-FI}^{max}(\mathbf{X}) + 0.015 \leq 0 \qquad \text{(D.13)}$$

with $\delta_{A-FI}^{max}(\mathbf{X}) = \max_{i,j}[\delta_{A-FI}(\mathbf{X}, t_i + t_j)]$ and $t_i + t_j$ as defined in Section D.3.3.2. Since the radius of the spring loaded lateral stiffener is 15 mm, a value of 0.015 m is assigned to the allowable perpendicular distance $\left|\delta_{A-FI}^{allow}\right|$ in the above expression. Note also that expression (D.13) corresponds to inequality (D.8) derived for the general situation depicted in Figure D.5.

D.3.3.4 Right hand frame boundary

The *right hand frame boundary* restricts point B on the moving platform to the left hand side of line GH in Figure D.7. Point B on the moving platform (body 1 in Figure D.2) is at local coordinates $(\xi^B, \eta^B)_1 = \left(\frac{X_1}{2}, 0\right)$ (see Section D.2.1). Line GH on the frame (body 8 in Figure 2.5) is treated here in a similar manner to line FI of the left hand frame boundary (see Section D.3.3.3) with the specification

that $[x_8, y_8, \phi_8]^T = \left[0,0,\frac{\pi}{2}\right]^T$. The global x-coordinate of line GH is $x^{GH} = X_4 + X_5 + 0.4$, from which the local η-coordinate, $\eta_8^{GH} = -(X_4 + X_5 + 0.4)$, may be determined (see expression (D.4)).

Note that since the perpendicular distance between line GH and point B becomes *smaller* as the platform moves closer to the right hand frame boundary, the *right hand frame boundary inequality constraint* is given by

$$C_{13}(\mathbf{X}) \equiv 0.015 - \delta_{B-GH}^{min}(\mathbf{X}) \leq 0 \qquad (D.14)$$

with $\delta_{B-GH}^{min}(\mathbf{X}) = \min_{i,j}[\delta_{B-GH}(\mathbf{X}, t_i + t_j)]$, and $\delta_{B-GH}(\mathbf{X}, t_i + t_j)$ solved for in accordance with expression (D.6) at each time instant $t_i + t_j$. Once again, an allowable perpendicular distance $\left|\delta_{B-GH}^{allow}\right| = 0.015\,m$ is specified to compensate for the 15 mm radius of the spring loaded lateral stiffener (see **Chapter 5**).

D.3.4 Revolute joint mechanical interference constraints

There are no explicit constraints specified for the relative rotations about the revolute joints of the hypothetical platform. In practice however, the allowable rotations about the revolute joints of the physical test-model are limited as a result of mechanical interferences.

The design and assembly of the test-model is explained in detail in **Chapter 5**. Figure D.10 shows an annotated two-dimensional view of the planar Gough-Stewart platform test-model, where the different components involved in the revolute joint mechanical interferences are annotated.

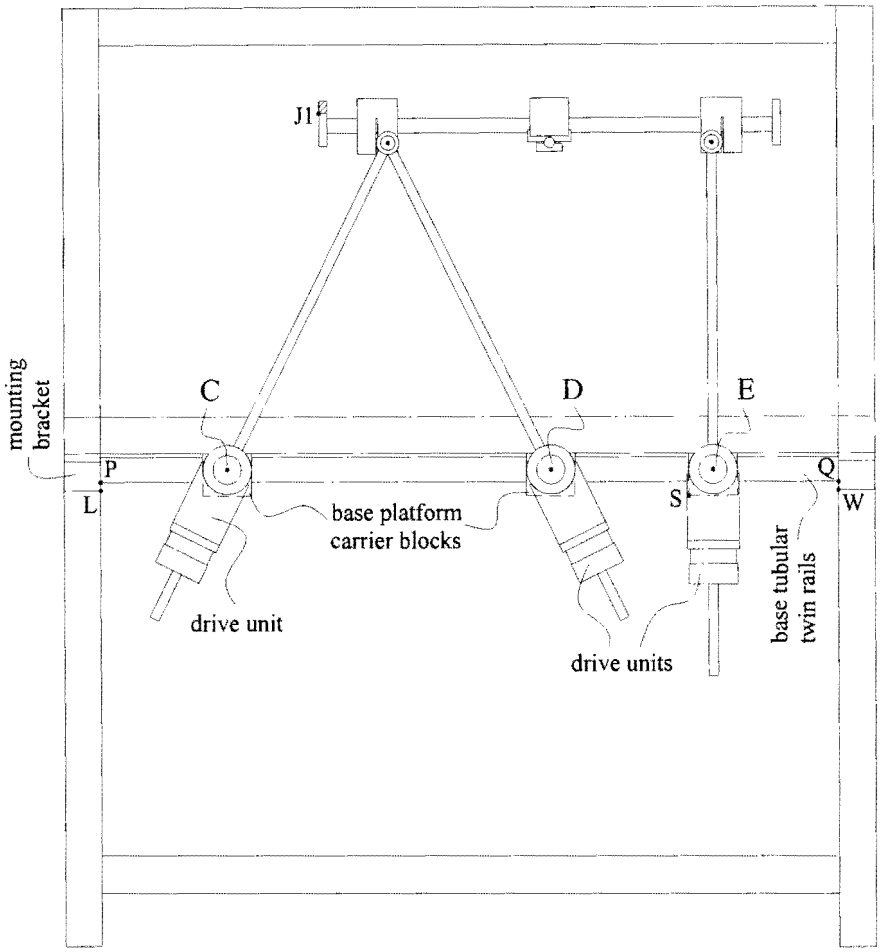

Figure D.10: Annotated drawing of the planar Gough Stewart platform test-model.

Consider for the moment the fixed base platform assembly. In essence, and with reference to Figure D.10 each of the three revolute joints C, D and E is connected to a pair of *carrier blocks*, which are linearly adjustable along the *base tubular twin rails*. These base tubular twin rails are connected to the frame by means of *mounting brackets*. The base revolute joints C, D and E carry the actuator leg *drive units*, each consisting of a motor and gearbox assembly.

Varying the actuator leg lengths, not only causes the moving platform to change its position and orientation, but also causes the relative orientations of the actuator legs to vary. The relative orientations of the actuator legs and drive units correspond exactly, hence the potential danger exists of mechanical interference between the drive units and the different components of the fixed base frame.

D.3.4.1 Revolute joint C mechanical interference constraints

The relative position of revolute joint C on the base tubular twin rails is determined by design variable X_2 (see Section D.2.1). Depending on the magnitude of X_2, an excessively large CW rotation of

actuator leg 1 will cause the drive unit carried by revolute joint C to collide with either the left hand mounting brackets, or with the base tubular twin rails.

The proposed inequality constraint methodology for the prevention of mechanical interference (Section D.3.1) may however be applied here to formulate two separate inequality constraints with which both potential collisions may be avoided:

$$C_{14}(\mathbf{X}) \equiv \delta^{max}_{M1-PQ}(\mathbf{X}) + 0.005 \leq 0 \tag{D.15}$$

$$C_{15}(\mathbf{X}) \equiv 0.005 - \delta^{min}_{L-M1M2}(\mathbf{X}) \leq 0 \tag{D.16}$$

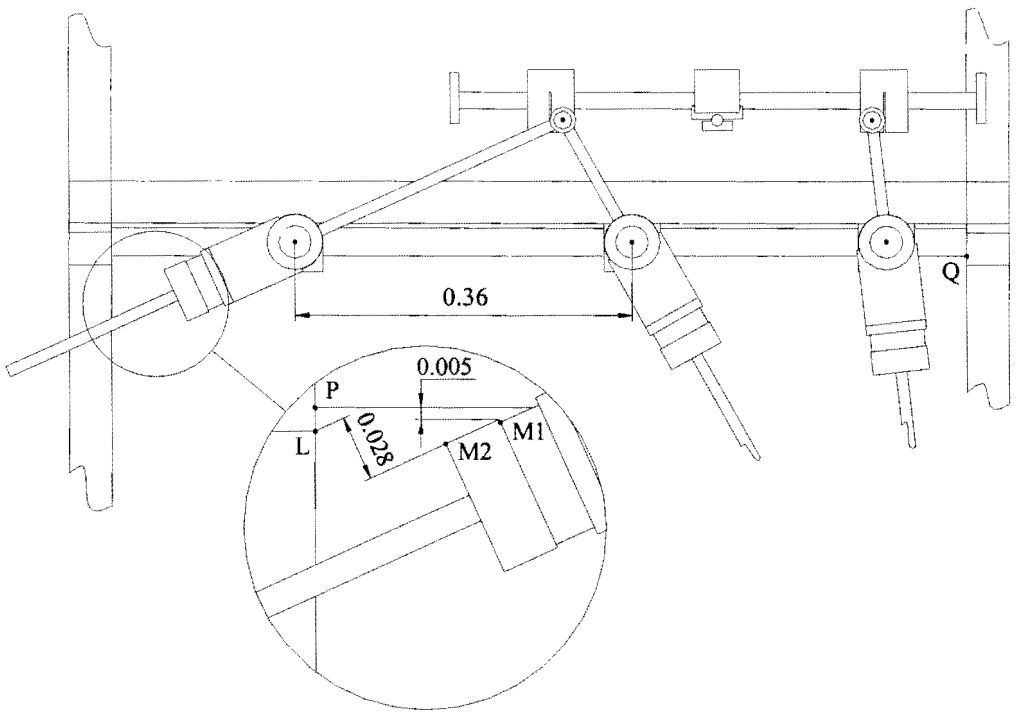

Figure D.11: Inequality constraint C_{14} (expression (D.15)) active.

Figure D.11 shows a scaled two-dimensional view of the test-model with $X_2 = 0.360\,\text{m}$, where drive unit C is about to collide with the base twin tubular rails, but *not* with the mounting brackets. Note that the perpendicular distance between line PQ and point M1 is $\delta_{M1-PQ} = 0.005\,\text{m}$, rendering inequality constraint C_{14} (expression (D.15)) active. In spite of this, the perpendicular distance between line M1M2 and point L is $\delta_{L-M1M2} = 0.028\,\text{m}$, so that inequality constraint C_{15} (expression (D.16)) is not active.

The evaluation of inequality constraints C_{14} is summarized in Table D.2 below:

General case analogy	**Inequality constraint C_{14}**
$\delta_{P-QR}^{max} \le -\left\|\delta_{P-QR}^{allow}\right\|$ (expression (D.8))	$C_{14}(\mathbf{X}) \equiv \delta_{M1-PQ}^{max}(\mathbf{X}) + 0.005 \le 0$ (expression (D.15))
Figure D.5	Figure D.11
Assumption 1: (see Section D.3.1)	
$[x, y, \phi]_i^T$ must be known	$[x, y, \phi]_5^T$ known from the inverse kinematic analysis (see Section 2.5)
$[x, y, \phi]_j^T$ must be known	$[x, y, \phi]_8^T = [0,0,0]^T$ fixed frame position and orientation (see Figure D.2)
Assumption 2: (see Section D.3.1)	
$(\xi^P, \eta^P)_i$ must be known	$(\xi^{M1}, \eta^{M1})_5 = (-0.06439, 0.03)$ (see Figure D.13)
Assumption 3: (see Section D.3.1)	
η_j^{QR} must be known	$\eta_8^{PQ} = X_3 - 0.015$

Table D.2: Evaluation of constraint C_{14} (expression (D.15)).

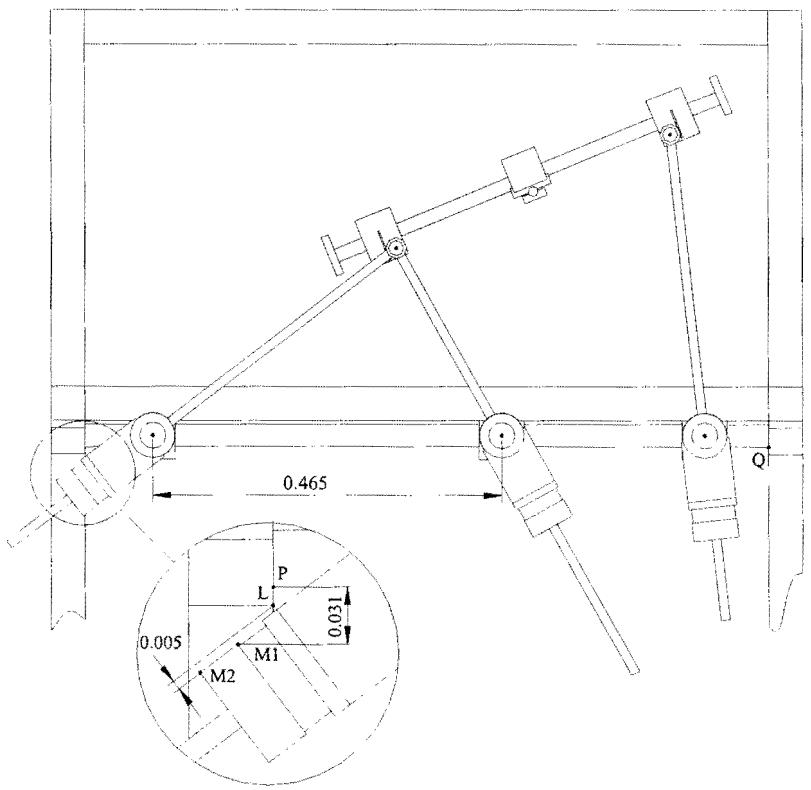

Figure D.12: Inequality constraint C_{15} (expression (D.16)) active.

On the other hand, Figure D.12 shows a scaled two-dimensional view of the test-model with $X_2 = 0.465\,\text{m}$, where drive unit C is about to collide with the left hand mounting bracket, and *not* with the base twin tubular rails. As expected, the perpendicular distance between line PQ and point M1, is greater than $0.005\,\text{m}$ ($\delta_{M1-PQ} = 0.031\,\text{m}$) so that inequality C_{14} (expression (D.15)) is *not* active, while $\delta_{L-M1M2} = 0.005\,\text{m}$, so that inequality C_{15} (expression (D.16)) becomes active.

The evaluation of inequality constraint C_{15} are summarized in Table D.3 below:

General case analogy	**Inequality constraint C_{15}**
$\left\|\delta_{P-QR}^{allow}\right\| \le \delta_{P-QR}^{min}$ (expression (D.7))	$C_{15}(\mathbf{X}) \equiv 0.005 - \delta_{L-M1M2}^{min}(\mathbf{X}) \le 0$ (expression (D.16))
Figure D.4	Figure D.12
Assumption 1: (see Section D.3.1)	
$[x,y,\phi]_i^T$ must be known	$[x,y,\phi]_8^T = [0,0,0]^T$ fixed frame position and orientation (see Figure D.2)
$[x,y,\phi]_j^T$ must be known	$[x,y,\phi]_5^T$ known from the inverse kinematic analysis (see Section 2.5)
Assumption 2: (see Section D.3.1)	
$(\xi^P,\eta^P)_i$ must be known	$(\xi^L,\eta^L)_8 = \left((X_4 + X_2 - 0.555),(X_3 - 0.025)\right)$
Assumption 3: (see Section D.3.1)	
η_j^{QR} must be known	$\eta_5^{M1M2} = 0.03$ (see Figure D.13)

Table D.3: Evaluation of constraint C_{15} (expression (D.16)).

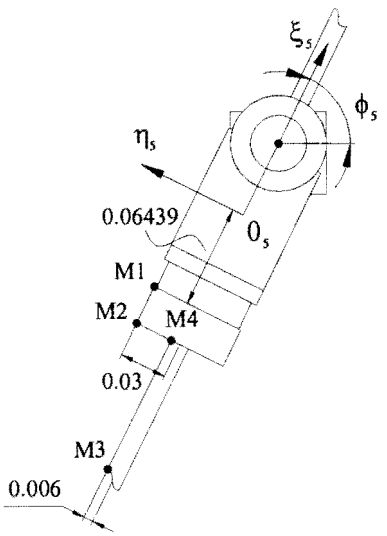

Figure D.13: Local coordinates on drive unit C.

D.3.4.2 Revolute joint D mechanical interference constraints

The relative position of revolute joint D on the base twin tubular rails is fixed (see Section D.2.1). However, the adjustable relative position of revolute joint E, given by the magnitude of design variable X_5, influences whether drive unit D will collide with the base twin tubular rails, or with the carrier blocks of revolute joint E. These potential collisions will of course only occur for excessively large CCW rotations of actuator leg 2. A third possible collision may occur between actuator leg 2 and drive unit E, depending on the value of X_5, as well as the relative orientations of actuator legs 2 and 3.

In order to prevent all three potential collisions from happening, three inequality constraints are formulated (refer to the annotations in Figure D.10 and Figure D.14 respectively):

$$C_{16}(\mathbf{X}) \equiv \delta^{max}_{R1-PQ}(\mathbf{X}) + 0.005 \leq 0 \tag{D.17}$$

$$C_{17}(\mathbf{X}) \equiv \delta^{max}_{S-R1R2}(\mathbf{X}) + 0.005 \leq 0 \tag{D.18}$$

$$C_{18}(\mathbf{X}) \equiv \delta^{max}_{T5-R3R4}(\mathbf{X}) + 0.005 \leq 0 \tag{D.19}$$

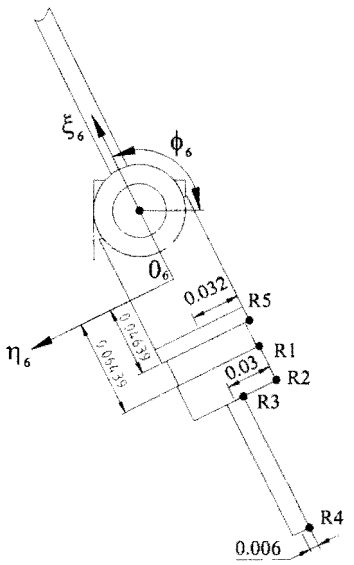

Figure D.14: Local coordinates on drive unit D.

D.3.4.3 Revolute joint E mechanical interference constraints

As previously stated in Sections D.2.1 and D.3.4.2, the magnitude of design variable X_5 determines the relative position of revolute joint E on the base twin tubular rails. For an extreme CCW orientation of actuator leg 3, and depending on the magnitude of design variable X_5, drive unit E will collide either with the base twin tubular rails, or with the right hand mounting bracket. There also exists the possibility of mechanical interference between actuator leg 3 and drive unit D, depending on the magnitude of design variable X_5, and the relative orientations of actuator legs 2 and 3.

Following the same recipe as before, three inequality constraint equations are formulated to prevent the above mentioned potential collisions from happening (refer to the annotations in Figure D.10 and Figure D.15 respectively):

$$C_{19}(\mathbf{X}) \equiv \delta^{max}_{V1-PQ}(\mathbf{X}) + 0.005 \leq 0 \tag{D.20}$$

$$C_{20}(\mathbf{X}) \equiv \delta^{max}_{W-V1V2}(\mathbf{X}) + 0.005 \leq 0 \tag{D.21}$$

$$C_{21}(\mathbf{X}) \equiv 0.005 - \delta^{min}_{R5-T3T4}(\mathbf{X}) \leq 0 \tag{D.22}$$

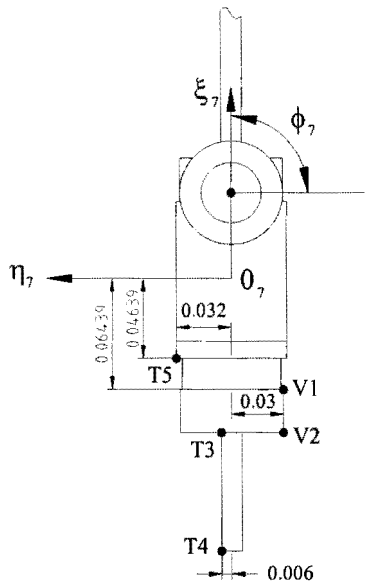

Figure D.15: Local coordinates on drive unit E.

D.3.4.4 Revolute joint A mechanical interference

Depending on the relative orientation of the moving platform (body 1 in Figure D.2) and actuator leg 1 (body 2 in Figure D.2), point J1 on the moving platform left hand bracket may collide with actuator leg 1. In order to avoid such a collision from happening, the following inequality constraint is formulated (see Figure D.16):

$$C_{22}(\mathbf{X}) \equiv 0.005 - \delta^{min}_{J1-M3M4}(\mathbf{X}) \leq 0 \tag{D.23}$$

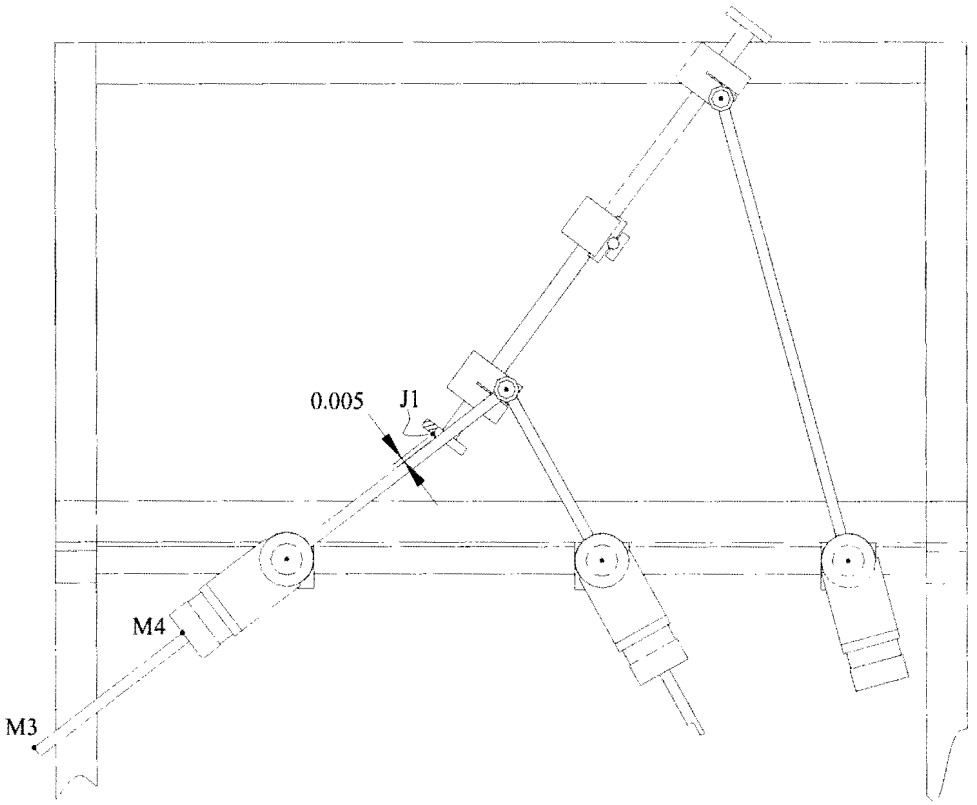

Figure D.16: Inequality constraint C_{22} (expression (D.23)) active.